

Metal-to-ligand and ligand-to-metal charge transfer in thin films of Prussian blue analogues investigated by X-ray absorption spectroscopy

Sébastien Bonhommeau,^{*a} Niko Pontius,^a Saioa Cobo,^b Lionel Salmon,^b
Frank M. F. de Groot,^c Gábor Molnár,^b Azzedine Bousseksou,^b
Hermann A. Dürr^a and Wolfgang Eberhardt^a

Received 22nd April 2008, Accepted 20th June 2008

First published as an Advance Article on the web 6th August 2008

DOI: 10.1039/b806783j

A series of thin films of Prussian blue analogues is investigated by X-ray absorption spectroscopy (XAS) at the Fe, Co and Mn L_{2,3}-edges. The ligand field multiplet theory enables us to examine accurately the electronic structure of these materials. Experimental XAS spectra of CoFe Prussian blue analogues are successfully reproduced using a ground state configuration including metal-to-ligand (MLCT) and ligand-to-metal charge transfer (LMCT) at the Co and Fe L_{2,3}-edges. In particular, a huge improvement is achieved for satellite peaks at the Co(III) L_{2,3}-edges compared to previous calculations in the literature based on LMCT effects only. On the other hand, XAS spectra of MnFe analogues synthesized for the first time, can be reproduced conveniently by taking into account either MLCT or LMCT depending on the conditions of the sample preparation. For each thin film, the proportion of the different oxidation states of Co, Fe and Mn is evaluated. Unexpectedly, this analysis reveals the presence of a significant amount of a reduced phase, which turns out to be strongly dependent on the sample synthesis and storage conditions.

1. Introduction

Valence-tautomeric Prussian blue analogues have attracted tremendous interest because of their various spectacular magnetic properties, such as high Curie temperatures,¹ first order thermal phase transitions² and photomagnetic effects.^{3,4-10} Their general formula is A_xM[M'(CN)₆]_y·nH₂O where A is an alkali metal cation and M and M' are divalent or trivalent transition metal cations. In this class, we are interested in the so-called CoFe and MnFe Prussian blue analogues in reference to the metal ions they contain.⁴ These compounds crystallize in face-centred cubic (fcc) structures. They consist of a 3D coordination network containing Fe(II)–CN–M(III) (M = Mn, Co) entities in their low-temperature (LT) phase and Fe(III)–CN–M(II) entities in their high-temperature (HT) phase. A number of Fe(CN)₆ sites are however vacant^{5,11} and filled by water molecules that bond to M ions through their O atoms.¹² Noncoordinated water molecules are often observed as well. In this lattice, additional alkali metal ions fill a few tetrahedral, interstitial sites.^{5,13} CoFe Prussian blue analogues typically undergo a thermal transition from the Fe(III)(S = 1/2)–CN–Co(II)(S = 3/2) HT phase to the Fe(II)(S = 0)–CN–Co(III)(S = 0) LT phase. The charge transfer between Fe and Co ions is consequently accompanied by a spin crossover at the Co ions from Co(II) in the high spin

(HS) state to Co(III) in the low spin (LS) state. On the contrary, MnFe Prussian blue analogues show a thermally induced phase transition from the HT cubic Fe(III)(S = 1/2)–CN–Mn(II) (S = 5/2) phase to the LT tetragonal Fe(II)(S = 0)–CN–Mn(III) (S = 2) phase accompanied by a Jahn–Teller distortion on the manganese ion.^{13,14}

Until now many investigations have been performed on these materials using X-ray techniques, such as X-ray diffraction,^{9,13,15} X-ray absorption spectroscopy^{5-7,10,12,16,17} and X-ray magnetic circular dichroism.⁸ However, these studies focused on powder samples and no X-ray data are available so far for Prussian-blue-based thin films. In this paper, we present the first X-ray absorption spectroscopy (XAS) measurements on a series of *ca.* 50 nm-thin films of CoFe and MnFe type Prussian blue analogues. The preparation of thin layers of Prussian blue analogues was accomplished by assembling multilayers on surfaces using alternate adsorption of cations and anions.¹⁸ In the past, this sequential assembly method has been explored on a variety of materials¹⁹ and allowed the deposition of dense, ultrathin films of Prussian blue and its analogues on various supports, with precise control over the thickness on the nanometer scale.²⁰ Using simulations based on the ligand field multiplet (LFM) theory,²¹ we show that the coexistence of metal-to-ligand charge transfer (MLCT) and ligand-to-metal charge transfer (LMCT) explains the absorption properties of CoFe analogues at both the Fe and the Co L_{2,3}-edges. Concerning MnFe Prussian blue analogues, the interplay between the observed charge transfer properties and the novel synthesis carried out is emphasized. In each case, the composition of the thin films is evaluated through the LFM simulations.

^a BESSY GmbH, Albert-Einstein-Str. 15, 12489 Berlin, Germany.
E-mail: bonhommeau@bessy.de; Fax: +49-30/6392-2136

^b Laboratoire de Chimie de Coordination, UPR 8241 CNRS, 205 route de Narbonne, F-31077 Toulouse cedex, France

^c Department of Inorganic Chemistry and Catalysis, Utrecht University, Sorbonnelaan 16, 3584 CA Utrecht, Netherlands

2. Experimental and calculation details

2.1 Sample preparation

All chemicals were of analytical grade and used without further purification. $K_3[Fe(CN)_6]$, $MnCl_2 \cdot 4H_2O$ and $RbCl$ were purchased from Sigma-Aldrich; $CoCl_2 \cdot 6H_2O$ and $NaCl$ were purchased from Fluka. The exact composition of the multilayer assemblies could not be obtained, that is the reason why samples will be named: $RbCoFe$, $NaCoFe$ and $RbMnFe$.

Thin films of $RbCoFe$ were assembled on 150 nm-thick Si_3N_4 membrane embedded in a silicon wafer (Silson Ltd) as follows (Fig. 1): the membrane was soaked alternately (total of 25 cycles) in 50 mM water solution of $CoCl_2 \cdot 6H_2O$ (1 min), then in a water solution containing both 50 mM $K_3[Fe(CN)_6]$ and 100 mM $RbCl$ (1 min) at room temperature, with two rinsing phases in water between the two steps during 30 s (method 1). Finally, they were dried under Ar flow. Raman measurements reveal the presence of two broad bands centred at 2100 and 2142 cm^{-1} which can be tentatively assigned to the reduced form $Co(II)-NC-Fe(II)$ and/or the LT component $Co(III)-NC-Fe(II)$.

The same method 1 was used for the elaboration of the corresponding $NaCoFe$ thin films but led to the formation of the totally reduced form. In order to limit the formation of this undesired form, a new method was developed: the membrane was soaked alternately in 50 mM water solution of $CoCl_2 \cdot 6H_2O$ (10 s), then in a water solution containing both 50 mM $K_3[Fe(CN)_6]$ and 100 mM $NaCl$ (10 s) at room temperature, with two rinsing phases in water between the two steps for 5 s; the six steps were carried out only 5 times (method 2). Finally, they were dried under Ar flow. Immediately after the deposition of the compound, Raman spectrum only shows a band at 2178 cm^{-1} assigned to the stretching cyano modes of the HT phase $Co(II)-NC-Fe(III)$ but evolution of the sample with time lead to the emergence of the corresponding modes at 2095 and 2143 cm^{-1} attributed to the reduced and LT phases and the concomitant disappearance of the HT phase.

Conversely the use of both method 1 or method 2 for the formation of thin films of $RbMnFe$ led unrelentingly to the formation of the totally reduced $Mn(II)-NC-Fe(II)$ pairs ($RbMnFe1$). As a consequence, a third method was used: the membrane was soaked alternately (total of 5 cycles) in

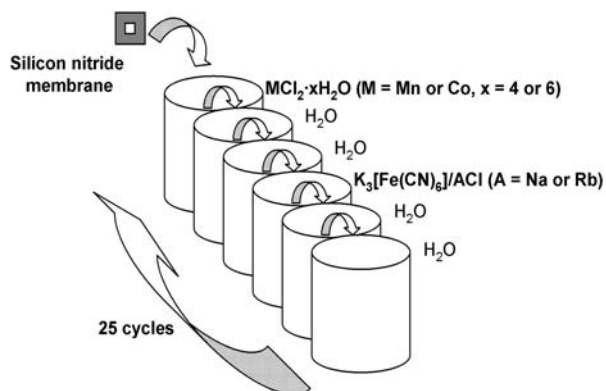


Fig. 1 Schematic representation of the multilayer sequential assembly.

15 mM water solution of $MnCl_2 \cdot 4H_2O$ (10 s), then in a water solution containing both 15 mM $K_3[Fe(CN)_6]$ and 20 mM $NaCl$ (10 s) at room temperature; no rinsing phase was realized between the two steps. Finally, they were dried under Ar flow. Raman spectrum exhibits two bands at 2159 and 2169 cm^{-1} which have been assigned to the HT pairs $Mn(II)-NC-Fe(III)$ ($RbMnFe3$).¹¹ Another sample similarly obtained was let in an oven at 125 °C during 1 week. The composition moved from a pure HT form to a mixture of both the HT, the LT $Mn(III)-NC-Fe(II)$ and the reduced $Mn(II)-NC-Fe(II)$ forms ($RbMnFe2$) as suggested by the appearance of two broad bands centred at 2090 and 2133 cm^{-1} in Raman spectra.^{11†} We can note that this time evolution is influenced by the water content which cannot be really controlled during the synthesis but varies also depending on the experimental conditions (vacuum, nitrogen atmosphere or air).

2.2 X-Ray absorption spectroscopy

Mn, Fe and Co $L_{2,3}$ -edges were recorded at the soft X-ray BESSY II beamline UE56/1-PGM-A. The photon flux of the full X-ray beam was typically reduced by a factor of 20, *i.e.* to around 10^{16} photons $cm^{-2} s^{-1}$, to avoid the degradation of the samples. All experiments were carried out in transmission geometry, which required deposition of Prussian blue analogues on very thin substrates. 150 nm-thick silicon nitride membranes were selected as substrates because of the high X-ray transmission of this material in the spectral region where Mn, Fe and Co $L_{2,3}$ -edges appeared. Regarding the number of cycles used during the multilayer sequential assembly the thickness of the thin films was evaluated to be *ca.* 50 nm. All the reported spectra were measured under a vacuum of about 10^{-8} mbar at 300 K. Measurements down to 70 K were also realised but they did not show any change compared to data collected at 300 K. For comparison with simulations, the baseline was subtracted (whenever needed) by using a linear function fitted to the data below the L_3 -edge region and beyond the L_2 -edge region.

2.2 Ligand field multiplet calculations

In order to extract quantitative information from $L_{2,3}$ -edges absorption spectra, experimental XAS spectra were modelled using the so-called ligand field multiplet (LFM) theory developed by Thole²¹ in the framework established by Cowan²² and Butler.²³ This approach takes into account all the electronic Coulomb interactions as well as the spin-orbit coupling on any electronic open shell and treats the geometrical environment of the absorbing atom through crystal field potential. The spectrum is calculated as the sum of all possible localized transitions in atoms for an electron excited from the 2p level to a 3d level. No attention is paid to the electric dipole allowed $2p \rightarrow 4s$ transitions that are experimentally and theoretically found to be negligible compared to the $2p \rightarrow 3d$ main channel. In the simplest formulation, a pure $3d^n$ configuration is attributed to the 3d transition ions in the ground state and

† Raman spectroscopy does not allow distinguishing the $Mn(II)-NC-Fe(III)$ pairs observed in $RbMnFe_2$ and $RbMnFe_3$, contrary to XAS measurements.

transitions between $2p^63d^n$ ground state and $2p^53d^{n+1}$ final excited state are calculated. The inter-electronic repulsions are introduced through Slater–Condon integrals, F_{dd}^2 and F_{dd}^4 for the initial state and F_{dd}^2 , F_{dd}^4 , F_{pd}^2 , G_{pd}^1 and G_{pd}^3 for the final state. The Slater–Condon integrals are calculated through an atomic Hartree–Fock model and are scaled down by a reduction factor κ which reflects the electronic delocalisation and the covalence of the chemical bonds. The atomic spin–orbit coupling parameters, ζ_{3d} and ζ_{2p} , are calculated considering the mono-electronic potential around the ion. The octahedral surrounding of the metal ion is represented by an octahedral (O_h) crystal field potential whose strength is parameterized by $10Dq$. For a tetragonal (D_{4h}) crystal field, in case of Jahn–Teller distortions for instance, two other parameters must be added, namely Ds and Dt , to account for the deformation. At this point hybridization is only present through the reduction factor κ and the ligand–metal charge transfer is not taken into account. To model LMCT effects the ground state of a $3d^n$ ion is taken to be a linear combination of two appropriate configurations, $3d^n$ and $3d^{n+1}\underline{L}$, where $3d^{n+1}$ stands for an extra $3d$ electron coming from the ligands and \underline{L} for the corresponding hole on a ligand orbital. For MLCT, the ground state configurations are $3d^n$ and $3d^{n-1}\underline{L}^-$ and when both MLCT and LMCT are considered three configurations are needed, $3d^{n-1}\underline{L}^-$, $3d^n$ and $3d^{n+1}\underline{L}$, where \underline{L}^- represents an extra electron originating from the metal ion. The parameters EG2 (EF2) and EG3 (EF3) determine the average energy separation between $3d^n$, $3d^{n+1}\underline{L}$ and $3d^{n-1}\underline{L}^-$ configurations in the ground (final) state. EG3 and EF3 are relevant only if three configurations are considered in the ground and final states. EG2 is the energy separation between $3d^n$ and $3d^{n+1}\underline{L}$ ($3d^n$ and $3d^{n-1}\underline{L}^-$) configurations for a LMCT (MLCT). When simulating both LMCT and MLCT, EG2 becomes the energy separation between $3d^{n-1}\underline{L}^-$ and $3d^n$ configurations and EG3 between $3d^{n-1}\underline{L}^-$ and $3d^{n+1}\underline{L}$ configurations. The strength of the charge transfer configurations $T(i)$ allows for the covalent overlap of different symmetry components (i). It is represented in octahedral symmetry by the two ligand–metal charge transfer integrals $T(t_{2g})$ and $T(e_g)$ and in tetragonal symmetry by the four integrals $T(b_{1g})$, $T(a_{1g})$, $T(b_{2g})$ and $T(e_g)$.²⁴

The purpose of the calculation lies in the computation of intensities of all possible transitions. In order to compare them to the experimental $L_{2,3}$ -edges XAS spectra, the theoretical transitions must be convoluted by a broadening function which takes into account the intrinsic core-hole lifetime and the instrumental resolution. In the following simulations, the full width at half maximum (FWHM) of the lifetime Lorentzian broadening function falls in the 0.2–0.4 eV energy range over the L_3 -edge and the 0.3–0.6 eV range over the L_2 -edge. The FWHM of the instrumental Gaussian broadening function is fixed at 0.2 eV. All simulations are carried out considering a temperature of 300 K.

3. XAS spectra of CoFe Prussian blue analogues

Fig. 2 provides the experimental XAS spectra and best simulations achieved for RbCoFe and NaCoFe at the Co and Fe $L_{2,3}$ -edges. The calculated XAS spectra accounting

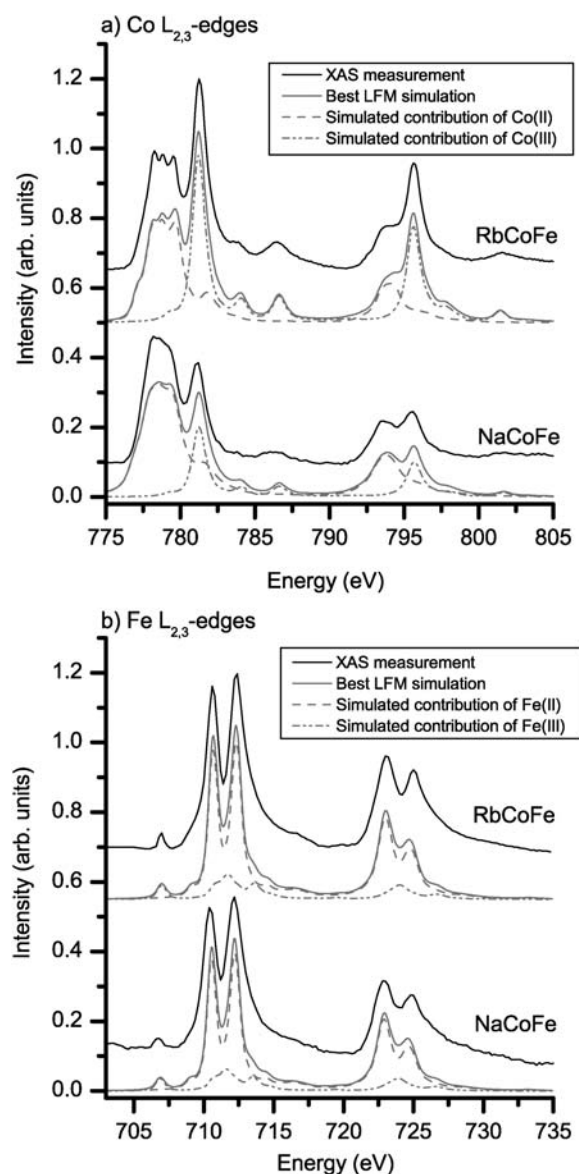


Fig. 2 Experimental XAS spectra recorded at 300 K and best simulations obtained for RbCoFe and NaCoFe at the Co $L_{2,3}$ -edges (a) and the Fe $L_{2,3}$ -edges (b). Simulations have been performed considering the ground state configurations 8% d^6L^- + 90% d^7 + 2% d^8L for Co(II) ions, 7% d^5L^- + 63% d^6 + 30% d^7L for Co(III) ions, 43% d^5L^- + 46% d^6 + 11% d^7L for Fe(II) ions and 32% d^4L^- + 53% d^5 + 15% d^6L for Fe(III) ions. For RbCoFe and NaCoFe, the linear combinations 50% [Co(II)] + 50% [Co(III)] and 75% [Co(II)] + 25% [Co(III)] have been used at the Co $L_{2,3}$ -edges, respectively, but the same linear combination that is 85% [Fe(II)] + 15% [Fe(III)] at the Fe $L_{2,3}$ -edges.

for experimental observations in these two materials are obtained by means of the same set of multiplet parameters (Table 1) except that the lifetime broadening is somewhat higher for the NaCoFe compound. This appears clearly through the lower resolved Co $L_{2,3}$ -edges in NaCoFe (Fig. 2a). The width and the different features of XAS spectra at the Co $L_{2,3}$ -edges constitute an evidence of the presence of Co ions in their oxidation state +II and +III. Peaks centred at 781.2, 783.9, 786.5, 795.6 and 801.5 eV are fingerprints of

Table 1 Ground state configurations and LFM parameters considered in order to reproduce the experimental spectra at the Co, Fe and Mn L_{2,3}-edges

	Co(II)	Co(III)	Fe(II)	Fe(III) ^b	Mn(II) ^c MnFeI	Mn(II) MnFe2
Ground state	⁴ T ₁ t _{2g} ⁵ e _g ²	¹ A ₁ t _{2g} ⁶ e _g ⁰	¹ A ₁ t _{2g} ⁶ e _g ⁰	² B _{2g} (² T ₂) e _g ⁴ b _{2g} ¹ b _{1g} ⁰ a _{1g} ⁰ (t _{2g} ⁵ e _g ⁰)	⁶ A ₁ e _g ² b _{2g} ¹ b _{1g} ¹ a _{1g}	⁶ A ₁ t _{2g} ³ e _g ²
κ/%	80	80	80	60	90	90
ζ _{2p} /eV	9.75	9.75	8.20	8.20	6.85	6.85
ζ _{3d} /eV	0.022	0.022	0.06	0.06	0.04	0.04
10Dq/eV	0.5	2.7	4.2	3.9	2.0	0.25
Dt/eV	—	—	—	-0.012	-0.25	—
Ds/eV	—	—	—	0	-0.2	—
EG2/eV	-5.0	-2.0	2.0	1.0	2.0	5.0
EF2/eV	-6.0	-3.0	0.5	0.5	3.0	3.0
EG3/eV	1.0	1.0	-2.0	1.0	—	—
EF3/eV	3.0	2.5	0	1.5	—	—
T(e _g) ML ^a	0	2.0	1.0	0.9	0/2.0	—
T(t _{2g}) ML ^a	0.7	1.2	1.9	2.2	0	—
T(e _g) LM ^a	1.0	3.5	0.9	2.1	—	2.0
T(t _{2g}) LM ^a	0	0	0	0.5	—	1.0

^a LM refers to the mixing between 3dⁿ and 3dⁿ⁺¹L and ML to the mixing between 3dⁿ and 3dⁿ⁻¹L⁻ configurations. ^b The ground state of Fe(III) is ²T₂ in O_h symmetry but ²B_{2g} in D_{4h} symmetry. In our simulations, T(e_g) = T(a_{1g}, D_{4h}) = T(b_{1g}, D_{4h}) and T(t_{2g}) = T(b_{2g}, D_{4h}) = T(e_g, D_{4h}). ^c T(b_{1g}, D_{4h}) = T(b_{2g}, D_{4h}) = T(e_g, D_{4h}) = 0 and T(a_{1g}, D_{4h}) = 2.0.

Co(III) ions in the LS state while peaks at 778.3, 778.8, 779.5 and 793.8 eV characterize Co(II) ions in the HS state.^{6,10,17}

The contribution of Co(II) ions is modelled using a weak crystal field of 0.5 eV compatible with the expected HS state. Even though a 100% d⁷ ground state configuration allows for the contribution of Co(II) ions in the XAS spectrum of CoFe Prussian blue analogues, the introduction of a 68% reduction factor of the Slater integrals κ turns out to be mandatory to improve the agreement between calculations and measurements at the Co L₃-edge in this case.^{6,10,17} In order to avoid the resort to this reduction, we chose the ground state configuration 8% d⁶L⁻ + 90% d⁷ + 2% d⁸L. Here, an MLCT and an LMCT are considered and the reduction factor is maintained at 80% in accordance with the usual reduction in electron repulsion of the experimental free ion value.²⁴ The low percentages of charge transfer configurations come from the relatively weak covalence of Co(II)-NC and Co(II)-O(H₂O) bonds.⁶ Through parameters listed in Table 1, this latter appears to be mainly due to some π back-donation (charge transfer from t_{2g} metal orbitals to the ligand) and σ donation (charge transfer from the ligand to the e_g metal orbitals). At this point, we need to emphasize that a small 3d spin-orbit coupling (ζ_{3d} = 0.022 eV) must be used to reproduce the energy position at the Co L₃-edge. The only way to compensate such decrease would be to bring the cubic crystal field down to almost 0 eV in complete disagreement with former investigations about Prussian blue analogues containing Co ions. This small 3d spin-orbit coupling is commonly assumed instead.^{6,10,16,17}

The contribution of Co(III) ions is modelled using the ground state configurations 7% d⁵L⁻ + 63% d⁶ + 30% d⁷L (Fig. 2a). Both MLCT and LMCT effects are included. This contrasts with former studies where only a LMCT was taken into account to simulate experimental XAS spectra of CoFe Prussian blue analogues.^{6,10,17} Fig. 3 demonstrates the effect of performing calculations using the optimised ground state configurations 62% d⁶ + 38% d⁵L⁻ (MLCT), 77% d⁶ +

23% d⁷L (LMCT) and 7% d⁵L⁻ + 63% d⁶ + 30% d⁷L (MLCT+LMCT) on the XAS spectrum of Co(III) ions. Significant changes appear for the satellite peaks at 786.5 eV and 801.5 eV. Their intensities are greatly overestimated if the calculation is limited to MLCT and underestimated for a LMCT alone. A right balance between MLCT and LMCT effects ensures on the contrary an almost perfect agreement with the experimental XAS spectra (Fig. 2a).

Considering this MLCT + LMCT approach, Co(III) ions are in the LS state due to the relatively high cubic crystal field of 2.7 eV (Table 1). Their t_{2g} orbitals are completely filled thereby. The π donation (charge transfer from the ligand to t_{2g} metal orbitals) is not likely to play any role accordingly (see T(t_{2g}) LM in Table 1). The π back-donation slightly

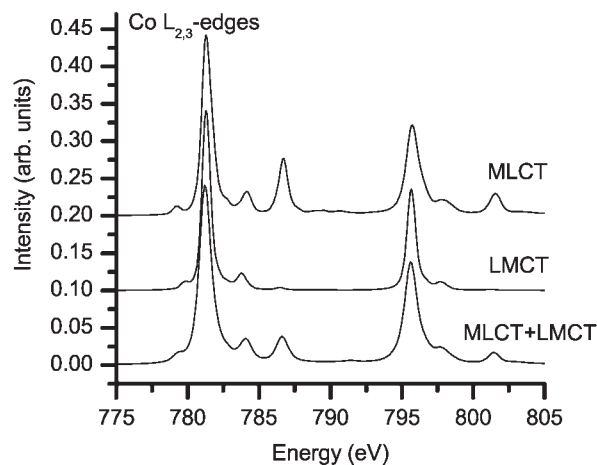


Fig. 3 LFM calculations at the Co L_{2,3}-edges using the ground state configurations 62% d⁶ + 38% d⁵L⁻ (MLCT), 77% d⁶ + 23% d⁷L (LMCT) and 7% d⁵L⁻ + 63% d⁶ + 30% d⁷L (MLCT+LMCT) for the XAS spectrum of Co(III) ions. Spectra are normalized with respect to the intense peak at 781.2 eV.

affects the energy position of the two aforementioned satellite peaks and should be taken into account hence. The strongest effect is generated, however, by the σ donation. All the peaks can be shifted in energy or significantly modified in intensity by varying it. This reveals the high covalence of Co(III)-ligand bonds. On the basis of calibrated intensities of reference compounds,^{25,26} the sum of the metal character in unoccupied d orbitals is indeed evaluated to be *ca.* 230%, which corresponds to 58% of metal character for each empty orbital of Co(III) ions in the LS state. Furthermore, this also explains why former studies on CoFe Prussian blue analogues focused on LMCT.^{10,17} To account for such strong covalence, Bleuzen and coworkers use additionally a reduction factor of the Slater integrals κ equal to 60% while a MLCT+LMCT calculation requires only an 80% factor, which is more reasonable as it has already been mentioned. Another effect supporting this latter approach lies in the σ back-donation from e_g metal orbitals to the ligand. Even though the e_g set of d orbitals in the ground state of LS Co(III) ions is empty, σ back-donation turns out efficient because, in an $L_{2,3}$ -edges X-ray absorption process, the excited state has $t_{2g}^6 e_g^1$ electron configuration, which has an e_g electron available to undergo σ back-bonding. This charge transfer allows fitting the energy separation between the satellite peaks and is indispensable to improve the agreement with experimental XAS spectra (Fig. 2a).

Crystal fields of Co ions also give information on their structure. As pointed out by Bleuzen *et al.*,^{12,17} Co(III)-NC-Fe(II) entities are linear. This implies a strong orbital interaction between Co ions and CN^- ligands and a strong Co ligand field ($10Dq = 2.7$ eV) leading to LS Co(III) ions. On the contrary, Co(II)-NC-Fe(III) entities should be bent because of 3D lattice strains. The much weaker orbital interaction between Co ions and CN^- ligands provides a weaker ligand field ($10Dq = 0.5$ eV) whose value is in line with what is expected in case of the formation of hydrogen bonds between H_2O bonded to Co and the CN^- ligand.¹⁷

The calculated spectrum of RbCoFe matches nicely the experimental spectrum when supposing the presence of 50% [Co(II)] + 50% [Co(III)]. On the other hand, we can estimate that NaCoFe films are filled by 75% [Co(II)] + 25% [Co(III)]. This difference cannot be explained in terms of the nature of the alkali ion. As the radius of the hydrated Na^+ cation is bigger than that of the hydrated Rb^+ cation,²⁷ the substitution of Rb^+ by Na^+ should indeed favour Co(III) ions in the LS state rather than Co(II) in the HS state for which antibonding e_g orbitals are populated leading to longer Co-NC bonds, that is a bigger volume of the coordination sphere of the Co ion. The predominance of Co(II) ions in NaCoFe is more likely due to a bigger amount of $[Fe(CN)_6]^{3-}$ or $[Fe(CN)_6]^{4-}$ vacancies yielding a smaller quantity of alkali ions in NaCoFe compared to RbCoFe in order to preserve the electroneutrality.¹¹ Such depletion in the number of Na^+ ions releases space, which favours HS species.

Measured XAS spectra plotted in Fig. 2b at the Fe $L_{2,3}$ -edges strikingly look like the XAS spectrum of LS Fe(II) ions in $K_4[Fe(CN)_6]$ reported earlier.²⁶ Relative intensities and energy position of peaks at 710.7, 712.3, 723.1 and 725 eV nicely match indeed. A more accurate comparison between calculated and experimental XAS spectra reveals however the

coexistence of the two oxidation states +II and +III for Fe ions in thin films of CoFe Prussian blue analogues. The peak around 707 eV associated with the $2p^6 t_{2g}^5 e_g^0 \rightarrow 2p^6 t_{2g}^4 e_g^1$ transition is effectively characteristic of LS Fe(III) since it is absent for LS Fe(II) ions having no vacant t_{2g} orbitals in their ground state in octahedral symmetry.

To reproduce experimental spectra, simulations including both MLCT and LMCT are performed as suggested by Hocking *et al.*²⁶ for $K_4[Fe(CN)_6]$ and $K_3[Fe(CN)_6]$ since Prussian blue analogues contain both $Fe(CN)_6$ entities. The cubic crystal field around 4 eV is compatible with Fe ions in the LS state (Table 1). The $10Dq$ value of Fe(II) coincides especially well with the 4.19 eV reported in the literature for $[Fe(CN)_6]^{4-}$.²⁸ The ground state configuration yielding the best accord with measurements is 43% $d^5 L^-$ + 46% d^6 + 11% $d^7 L$ for Fe(II) ions and 32% $d^4 L^-$ + 53% d^5 + 15% $d^6 L$ for Fe(III) ions. In thin films, the proportion of $d^5 L^-$ configuration is somewhat higher and that of $d^7 L$ is lower than previously observed for $Fe(CN)_6^{4-}$.²⁶ Nevertheless, in both cases, the main effect is the π back-donation coming from the MLCT mixing into $CN^- \pi^*$ orbitals of t_{2g} symmetry. Furthermore, σ back-donation into σ^* molecular orbitals of the CN^- ligand and σ donation affect the spectra as well.²⁶

The Fe $L_{2,3}$ -edges of the XAS spectra of RbCoFe and NaCoFe are well reproduced by means of the linear combination 85% [Fe(II)] + 15% [Fe(III)]. It appears possible to ascribe the percentage of Fe(II) and Fe(III) sites in materials containing both ions owing to the striking difference between Fe(II) and Fe(III) XAS spectra. In particular, the quantity of LS Fe(III) ions can be determined by looking at the characteristic transition around 707 eV (Fig. 2b).

Investigations at the Co $L_{2,3}$ -edges show the presence of a 50% [Co(II)] + 50% [Co(III)] mixture and a 85% [Fe(II)] + 15% [Fe(III)] mixture at the Fe $L_{2,3}$ -edges in RbCoFe. We can therefore assess that this thin film contains *ca.* 35–50% diamagnetic Co(III)-NC-Fe(II) pairs corresponding to the LT phase, 35–50% reduced form Co(II)-NC-Fe(II), 0–15% Co(II)-NC-Fe(III) pairs associated to the HT phase and/or 0–15% oxidized form Co(III)-NC-Fe(III). For NaCoFe, the proportions 75% [Co(II)] + 25% [Co(III)] and 85% [Fe(II)] + 15% [Fe(III)] entail the coexistence of *ca.* 10–25% diamagnetic Co(III)-NC-Fe(II) pairs, 60–75% reduced form Co(II)-NC-Fe(II), 0–15% Co(II)-NC-Fe(III) pairs and/or 0–15% oxidized form Co(III)-NC-Fe(III).

4. XAS spectra of MnFe Prussian blue analogues

Fig. 4 exhibits the experimental XAS spectra and best simulations achieved for two MnFe Prussian blue analogues, called RbMnFe1 and RbMnFe2, at the Mn and Fe $L_{2,3}$ -edges. The presence of transitions at 639.0, 640.0, 641.4, 643.5, 650.4 and 652.3 eV strongly supports the presence of Mn(II) ions (Fig. 4a).²⁹ More precisely, measured and simulated XAS spectra of RbMnFe1 agree quite well if one considers Mn(II) ions in tetragonal symmetry ($Dt = -0.25$ eV and $Ds = -0.2$ eV) with the ground state configuration 70% d^5 + 30% $d^4 L^-$ (Fig. 4a), *i.e.* including the MLCT phenomenon. Any other attempt (with various sets of parameters and charge transfer effects) leads to a much worse accordance. In particular, assuming a contribution of Mn(III) ions, whose L_3 -edge is

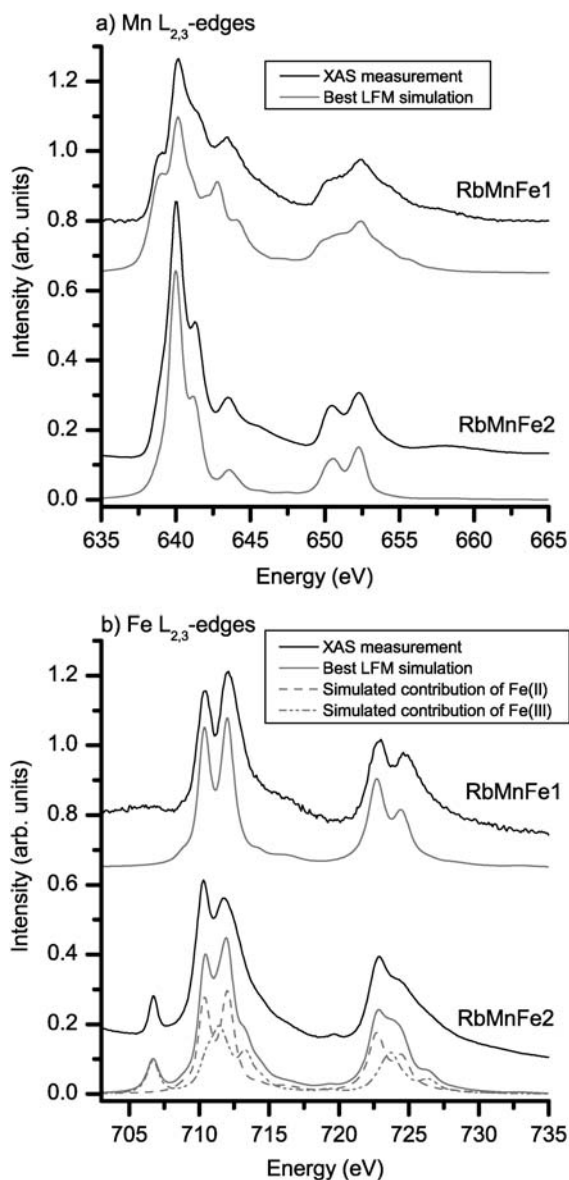


Fig. 4 Experimental XAS spectra recorded at 300 K and best simulations obtained for RbMnFe1 and RbMnFe2 at the Mn $L_{2,3}$ -edges (a) and the Fe $L_{2,3}$ -edges (b). Simulations have been performed considering the ground state configurations 70% $d^5 + 30\%$ d^4L^- for Mn(II) ions in RbMnFe1, 89% $d^5 + 11\%$ d^6L^- for Mn(II) ions in RbMnFe2, 43% $d^5L^- + 46\%$ $d^6 + 11\%$ d^7L^- for Fe(II) ions and 32% $d^4L^- + 53\%$ $d^5 + 15\%$ d^6L^- for Fe(III) ions. For RbMnFe2, the linear combination 60% [Fe(II)] + 40% [Fe(III)] has been used.

typically shifted to 1.5–2 eV upward with respect to the L_3 -edge of Mn(II) ions when they are bonded to the same ligands,³⁰ cannot wipe out the slight discrepancy between experiments and simulations. The latter might be rather ascribed to a state dependent lifetime broadening, which could not be taken into account in a unique way.³¹ Despite their surprising symmetry, Mn(II) ions remain in the HS state as expected for MnFe Prussian blue analogues. The only relevant charge transfer mixing parameter is associated to σ back-donation from the highest occupied a_{1g} orbitals of the metal ion to the CN^- ligand (Table 1).

While the synthesis of MnFe Prussian blue analogues is carried out with reactants composed of Mn(II) ions in octahedral symmetry and Fe(III) ions, the experimental XAS spectrum collected at the Fe $L_{2,3}$ -edges seems perfectly compatible with a Fe(II) content (Fig. 4b).²⁷ Simulations are performed by means of a 43% $d^5L^- + 46\%$ $d^6 + 11\%$ d^7L^- ground state configuration like for CoFe Prussian blue analogues. We can suggest that the reduction of Fe(III) sites into Fe(II) ions induces lattice strains, which modify the local surrounding of Mn(II) ions leading to the symmetry change. Although unusual, it has already been observed that such symmetry changes were possible during the reduction of Co ions.³²

The experimental XAS spectrum of RbMnFe2 can be reproduced by means of Mn(II) ions in octahedral symmetry with the ground state configuration 89% $d^5 + 11\%$ d^6L^- (Fig. 4a). Compared to RbMnFe1, transitions at 639.0 and 643.5 eV are both much weaker. The depletion at 639.0 eV originates from the lower cubic crystal field, 0.25 eV instead of 2.0 eV, which is probably related to a bigger amount of defects in the lattice. Indeed, unlike RbMnFe1, RbMnFe2 is prepared following a rapid synthesis able to generate an altered lattice. The difference at 643.5 eV is directly linked to the occurrence of a LMCT for RbMnFe2 instead of the MLCT observed for RbMnFe1. We can stress that the recorded XAS spectrum of RbMnFe2 is in fairly good agreement with previous studies realised on Mn-based organometallic compounds^{16,29,30} in spite of a weaker crystal field. In particular, both σ and π donation play an important role since metal e_g and t_{2g} orbitals are partly filled only in the HS ${}^6A_1(t_{2g}^3e_g^2)$ ground state of these Mn(II) ions (Table 1).

The XAS spectrum of RbMnFe2 matches the simulated spectrum obtained through a 60% [Fe(II)] + 40% [Fe(III)] mixture (Fig. 4b), where the ground state configurations are still 43% $d^5L^- + 46\%$ $d^6 + 11\%$ d^7L^- for Fe(II) ions and 32% $d^4L^- + 53\%$ $d^5 + 15\%$ d^6L^- for Fe(III) ions. A reduction of initial Fe(III) ions occurs like for RbMnFe1 but it appears less complete.

From the calculated proportions of Mn(II), Fe(II) and Fe(III) ions, we can conclude that RbMnFe1 is composed exclusively of reduced Mn(II)–NC–Fe(II) pairs whereas RbMnFe2 contains 60% of reduced Mn(II)–NC–Fe(II) pairs and 40% of Mn(II)–NC–Fe(III) pairs that can be assigned to the HT phase. At this point, it is worth reminding that the preparation of RbMnFe2 involves a thermal treatment. Without this, the thin film composition becomes drastically different. Fig. 5 displays XAS spectra collected at the Mn and Fe $L_{2,3}$ -edges in this case. LFM simulations suggest the exclusive presence of Fe(III) ions in the RbMnFe3 sample as it can be deduced from the existence of the strong transition around 707 eV (Fig. 5b). At the Mn $L_{2,3}$ -edges, they fail in reproducing the experimental XAS spectrum but a comparison with the simulation carried out for RbMnFe2 shows that only Mn(II) ions should be present (Fig. 5a). The double-structured L_2 -edge as well as the transitions at the L_3 -edge are fingerprints of the +II oxidation state observed also in RbMnFe1 and RbMnFe2. In RbMnFe3, mainly Mn(II)–NC–Fe(III) pairs are detected hence but they are definitely different from that constituting RbMnFe2.

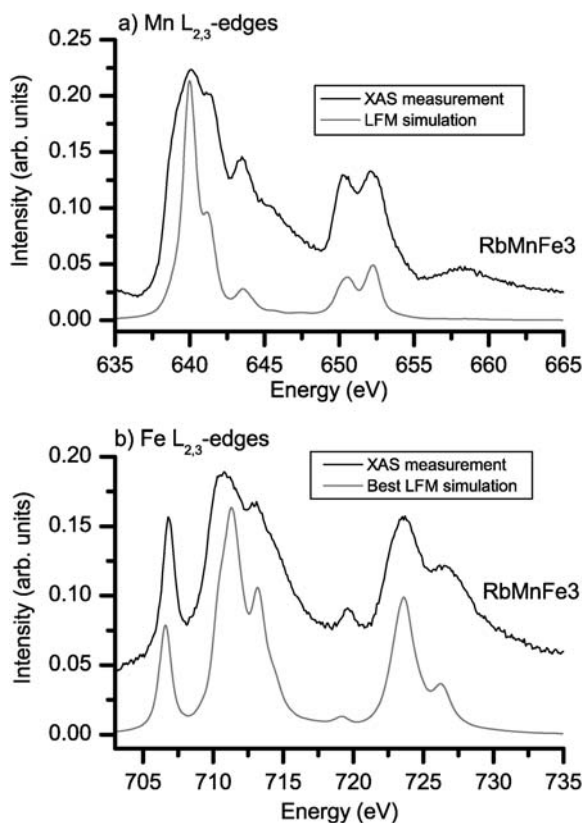


Fig. 5 Experimental XAS spectra recorded at 300 K and LFM simulations obtained for RbMnFe3 at the Mn $L_{2,3}$ -edges (a) and the Fe $L_{2,3}$ -edges (b). The calculated spectrum in (a) corresponds to the best simulation for RbMnFe2 (Fig. 4a). The simulation at the Fe $L_{2,3}$ -edges has been performed considering the ground state configuration 32% d^4L^- + 53% d^5 + 15% d^6L only, which reveals the exclusive presence of Fe(III) ions.

5. Conclusions

Thin films of CoFe and MnFe Prussian blue analogues have been synthesized for the first time on thin Si_3N_4 membranes. Such arrangement has rendered possible XAS studies in transmission geometry in order to investigate the electronic configuration of these materials. RbCoFe and NaCoFe Prussian blue analogues appear to contain a reasonable amount of Co(III)–NC–Fe(II) diamagnetic pairs and the XAS contribution of Co(III) ions appears to be strongly influenced by the CN^- ligand. At this ion both MLCT and LMCT effects are of paramount importance to reproduce satellite peaks that are known to be fingerprints of charge transfer phenomena.²⁴ Comparison with former studies^{10,17} shows that these diamagnetic pairs are linear and the RbCoFe film contain a higher amount of these pairs than the NaCoFe sample. This study of CoFe analogues reveals several similarities with powder samples famous for their photo-induced properties related to the presence of the Co(III)–NC–Fe(II) diamagnetic pairs,⁵ suggesting the interest of future photophysical investigations on these films.

Interestingly, in MnFe Prussian blue analogues, charge transfer properties at the Mn(II) ions were strongly dependent on the kinetics of the sample preparation. A sequential

assembly of the coordination network leads to Mn(II) ions in tetragonal symmetry and exhibiting MLCT (RbMnFe1), whereas a precipitation yields Mn(II) ions in octahedral symmetry where LMCT is dominant (RbMnFe2). Parallel to this change, a complete reduction of Fe(III) into Fe(II) ions is induced in the first case, but it is only partial in the second case and fully vanishes for RbMnFe3. Nevertheless, XAS measurements consist of snapshots of the electronic states and further evolution of the thin films (RbMnFe2 and RbMnFe3) with time cannot be excluded—as it has been inferred from Raman measurements. On the whole, however, this study indicates that charge transfer properties are tunable depending on the sample preparation conditions, even though many details about the relation between the synthesis method and the physical properties are still under investigation.

Acknowledgements

We are indebted to the BESSY staff for their help whenever needed. Financial support by the DFG through SPP1133 is gratefully acknowledged.

References

- 1 T. Mallah, S. Thiébaud, M. Verdagner and P. Veillet, *Science*, 1993, **262**, 1554; S. Ferlay, T. Mallah, R. Ouhaès, P. Veillet and M. Verdagner, *Nature*, 1995, **378**, 701; M. Verdagner, A. Bleuzen, V. Marvaud, J. Vaissermann, M. Seuleiman, C. Desplanches, A. Scullier, C. Train, R. Garde, G. Gelly, C. Lomenech, I. Roseman, P. Veillet, C. Cartier and F. Villain, *Coord. Chem. Rev.*, 1999, **190–192**, 1023; S. M. Holmes and G. S. Girolami, *J. Am. Chem. Soc.*, 1999, **121**, 5593; Ø. Hatlevik, W. E. Buschmann, J. Zhang, J. L. Manson and J. S. Miller, *Adv. Mater.*, 1999, **11**, 914.
- 2 N. Shimamoto, S. Ohkoshi, O. Sato and K. Hashimoto, *Inorg. Chem.*, 2002, **41**, 678; S. Ohkoshi, T. Matsuda, H. Tokoro and K. Hashimoto, *Chem. Mater.*, 2005, **17**, 81; H. Tokoro, S. Miyashita, K. Hashimoto and S. Ohkoshi, *Phys. Rev. B*, 2006, **73**, 172415.
- 3 O. Sato, T. Iyoda, A. Fujishima and K. Hashimoto, *Science*, 1996, **272**, 704; A. Goujon, O. Roubeau, F. Varret, A. Dolbecq, A. Bleuzen and M. Verdagner, *Eur. Phys. J. B*, 2000, **14**, 115; T. Kawamoto, Y. Asai and S. Abe, *Phys. Rev. Lett.*, 2001, **86**, 348; H. W. Liu, K. Matsuda, Z. Z. Gu, K. Takahashi, A. L. Cui, R. Nakajima, A. Fujishima and O. Sato, *Phys. Rev. Lett.*, 2003, **90**, 167403; H. Tokoro, S. Ohkoshi and K. Hashimoto, *Appl. Phys. Lett.*, 2003, **82**, 1245; M. Nishino, K. Boukheddaden, S. Miyashita and F. Varret, *Phys. Rev. B*, 2005, **72**, 064452; F. Varret, K. Boukheddaden, E. Codjovi, I. Maurin, H. Tokoro, S. Ohkoshi and K. Hashimoto, *Polyhedron*, 2005, **24**, 2857.
- 4 O. Sato, J. Tao and Y. Z. Zhang, *Angew. Chem., Int. Ed.*, 2007, **46**, 2152.
- 5 A. Bleuzen, C. Lomenech, V. Escax, F. Villain, F. Varret, C. Cartier dit Moulin and M. Verdagner, *J. Am. Chem. Soc.*, 2000, **122**, 6648.
- 6 C. Cartier dit Moulin, F. Villain, A. Bleuzen, M. A. Arrio, P. Sainctavit, C. Lomenech, V. Escax, F. Baudet, E. Dartyge, J.-J. Gallet and M. Verdagner, *J. Am. Chem. Soc.*, 2000, **122**, 6653.
- 7 V. Escax, A. Bleuzen, C. Cartier dit Moulin, F. Villain, A. Goujon, F. Varret and Michel Verdagner, *J. Am. Chem. Soc.*, 2001, **123**, 12536.
- 8 G. Champion, V. Escax, C. Cartier dit Moulin, A. Bleuzen, F. Villain, F. Baudet, E. Dartyge and M. Verdagner, *J. Am. Chem. Soc.*, 2001, **123**, 12544.
- 9 V. Escax, A. Bleuzen, J. P. Itié, P. Munsch, F. Varret and M. Verdagner, *J. Phys. Chem. B*, 2003, **107**, 4763.
- 10 C. Cartier dit Moulin, G. Champion, J. D. Cafun, M. A. Arrio and A. Bleuzen, *Angew. Chem., Int. Ed.*, 2007, **46**, 1287.

- 11 S. Cobo, R. Fernández, L. Salmon, G. Molnár and A. Bousseksou, *Eur. J. Inorg. Chem.*, 2007, 1549.
- 12 A. Bleuzen, V. Escax, A. Ferrier, F. Villain, M. Verdagner, P. Münsch and J. P. Itié, *Angew. Chem., Int. Ed.*, 2004, **43**, 3728.
- 13 S. Ohkoshi, H. Tokoro, M. Utsunomiya, M. Mizun, M. Abe and K. Hashimoto, *J. Phys. Chem. B*, 2002, **106**, 2423.
- 14 K. Kato, Y. Moritomo, M. Takata, M. Sakata, M. Umekawa, N. Hamada, S. Ohkoshi, H. Tokoro and K. Hashimoto, *Phys. Rev. Lett.*, 2003, **91**, 255502.
- 15 Y. Moritomo, M. Hanawa, Y. Ohishi, K. Kato, M. Takata, A. Kuriki, E. Nishibori, M. Sakata, S. Ohkoshi, H. Tokoro and K. Hashimoto, *Phys. Rev. B*, 2003, **68**, 144106; S. Margadonna, K. Prassides and A. N. Fitch, *Angew. Chem., Int. Ed.*, 2004, **43**, 6316.
- 16 M. A. Arrio, P. Sainctavit, C. Cartier dit Moulin, T. Mallah, M. Verdagner, E. Pellegrin and C. T. Chen, *J. Am. Chem. Soc.*, 1996, **118**, 6422.
- 17 V. Escax, G. Champion, M. A. Arrio, M. Zacchigna, C. Cartier dit Moulin and A. Bleuzen, *Angew. Chem., Int. Ed.*, 2005, **44**, 4798.
- 18 G. Decher, *Science*, 1997, **277**, 1232; *Multilayer Thin Films*, ed. G. Decher and J. B. Schlenoff, Wiley-VCH, Weinheim, 2003.
- 19 S. Cobo, G. Molnár, J. A. Real and A. Bousseksou, *Angew. Chem., Int. Ed.*, 2006, **45**, 5786; C. M. Bell, S. W. Keller, V. M. Lynch and T. E. Mallouk, *Mater. Chem. Phys.*, 1993, **35**, 225; C. Lin and C. R. Kagan, *J. Am. Chem. Soc.*, 2003, **125**, 336.
- 20 R. C. Millward, C. E. Madden, I. Sutherland, R. J. Mortimer, S. Fletcher and F. Marken, *Chem. Commun.*, 2001, 1994; W. Jin, A. Toutianoush, M. Pyrasch, J. Schnepf, H. Gottschalk, W. Rammensee and B. Tieke, *J. Phys. Chem. B*, 2003, **107**, 12062; M. Pyrasch, A. Toutianoush, W. Jin, J. Schnepf and B. Tieke, *Chem. Mater.*, 2003, **15**, 245; J. T. Culp, J.-H. Park, I. O. Benitez, Y.-D. Huh, M. W. Meisel and D. R. Talham, *Chem. Mater.*, 2003, **15**, 3431.
- 21 B. T. Thole, G. van der Laan, J. C. Fuggle, G. A. Sawatzky, R. C. Karanatak and J. M. Esteve, *Phys. Rev. B*, 1985, **32**, 5107.
- 22 R. D. Cowan, *The Theory of Atomic Structure and Spectra*, University of California Press, Berkeley, 1981.
- 23 P. H. Butler, *Point group symmetry, Applications, Methods and Tables*, Plenum, New York, 1991.
- 24 F. de Groot, *Coord. Chem. Rev.*, 2005, **249**, 31; F. de Groot, *Chem. Rev.*, 2001, **101**, 1779.
- 25 E. C. Wasinger, F. M. F. de Groot, B. Hedman, K. O. Hodgson and E. I. Solomon, *J. Am. Chem. Soc.*, 2003, **125**, 12894.
- 26 R. K. Hocking, E. C. Wasinger, F. M. F. de Groot, K. O. Hodgson, B. Hedman and E. I. Solomon, *J. Am. Chem. Soc.*, 2006, **128**, 10442.
- 27 Y. Marcus, *Chem. Rev.*, 1988, **88**, 1475.
- 28 C. S. Naiman, *J. Chem. Phys.*, 1961, **35**, 323.
- 29 M. M. Grush, J. Chen, T. L. Stemmler, S. J. George, C. Y. Ralston, R. T. Stibrany, A. Gelasco, G. Christou, S. M. Gorun, J. E. Penner-Hahn and S. P. Cramer, *J. Am. Chem. Soc.*, 1996, **118**, 65.
- 30 S. P. Cramer, F. M. F. de Groot, Y. Ma, C. T. Chen, F. Sette, C. A. Kipke, D. M. Eichhorn, M. K. Chan, W. H. Armstrong, E. Libby, G. Christou, S. Brooker, V. McKee, O. C. Mullins and J. C. Fuggle, *J. Am. Chem. Soc.*, 1991, **113**, 7937.
- 31 K. Okada, A. Kotani, H. Ogasawara, Y. Seino and B. T. Thole, *Phys. Rev. B*, 1993, **47**, 6203.
- 32 F. Morales, F. M. F. de Groot, P. Glatzel, E. Kleimenov, H. Bluhm, M. Hävecker, A. Knop-Gericke and B. M. Weckhuysen, *J. Phys. Chem. B*, 2004, **108**, 16201.